Suplemento de la Revista Mexicana de Física **4** 011003 (2023) 1–6

GEANT4 dose estimations of solar protons: Al and PMMA-Bi_2O_3 shielding for space exploration

J. A. Mireles

Dept. of Physics, U. of Texas at El Paso, El Paso, TX, U.S.A.

J. A. López

Dept. of Physics, U. of Texas at El Paso, El Paso, TX, U.S.A.

L. Sajo-Bohus

U. Simón Bolívar, Valle de Sartenejas, Caracas, Venezuela,
Óbuda U., Alba Regia Eng. Dept, Székesfehérvár, Hungary.

M. Castro-Colin

Bruker AXS, Karslruhe, Germany.

Received 4 October 2022; accepted 15 December 2022

Adverse effects of long-term exposure to galactic cosmic radiation (GCR) pose a clear obstacle to future space exploration programs. In addition to GCR we have solar particle radiation. We simulated the latter using a scaled fluence profile of solar protons taken from a study in the literature that comprises about three solar cycles. The model is a three-layer stack that includes shielding material and muscular tissue. Our simulation strategy uses protons as precursor radiation of neutrons. Subsequently, the shield is adjusted for thickness, dictated by an average depth at which neutrons are created through various processes during the simulation. Neutrons are then energy-binned and a corresponding neutron flux is simulated. Particles generated during the second phase of the simulation, *i.e.* neutrons, are then counted toward absorbed dose within the muscular tissue layer. Clearly, the dynamics of the process is not captured by the simulation, nevertheless, both neutron yield and absorbed dose can be estimated. The objective is to provide some insight about the effect of the new composite shield, PMMA-Bi_2O_3, that has an inherent capability for gamma dose reduction, compared to a more traditional aluminum shield.

Keywords: Radiation; cosmic radiation; spectrometry; shielding materials; space exploration; monte-Carlo simulations.

DOI: https://doi.org/10.31349/SuplRevMexFis.4.011003

1. Introduction

Mars and the Moon are the most immediate targets for space exploration, regarding budget and distance, and they already pose a significant challenge. By that token, at the present time only the United States has completed manned missions to the Moon. Mars-manned landings will only happen in the near future. In the meantime only robotic exploration has been developed, with a sizable impact in the 1960s and a steady increase from the mid 1970s [1–3]. Interest in space exploration is not only scientific or societal, but also commercial [4, 5]. For the mining exploration business, Mars is relevant as a launching point to access Main Belt Asteroids (MBAs) [5]. Thus, multiple organizations have a variety of interests. Added to the efforts of NASA we have also those of the European Space Agency (ESA), the China National Space Agency (CNSA), the Indian Space Research Organization (ISRO), the United Arab Emirates Space Agency (UAESA), and other private organizations [3, 6]. At any rate, space exploration is one of humanity's future endeavors that is expected to continue evolving and while doing so forming a better perspective of the problem at hand. Scientists and engineers agree that among other concerns radiation is a paramount aspect [6, 7]. Especially for missions with long-time duration.

Galactic cosmic rays (GCR) and solar particle events (SPE) are the two main radiation sources of concern. Protons [8,9] constitute the main type of particle in both sources. It is understood that the most plausible candidates of GCR are supernova remnants [8], while the sudden release of magnetic energy during solar eruptions is considered to be responsible for solar particle production [10].

The present work is concerned with proton irradiation as a precursor of neutrons. Neutrons scatter elastically, inelastically, can be captured, and cause spallation. Detailed experiments about the radiation environment onboard the International Space Station (ISS) [11] indicate that the annual absorbed dose of space radiation can be greater than 400 times—compared to that on Earth-average, say about 0.3 mSv, in the U.S.A. [12]. More specifically, we looked at a study at the ISS [13], also with passive detectors—solid state nuclear track detectors—which registered about 20% neutron contribution to the absorbed dose. Not unexpectedly, a radiation field will gain complexity after interacting with a human dwelling or robotic enclosure when unprotected by the Earth.

Neutrons are neither part of the GCR nor the SPE. They are however spalled by both. Wilson *et al.* [14] have used neutrons generated by GCR spallation to measure the lifetime of the neutron—about 760 s—, which emphasizes the lack of neutrons in the GCR or SPE.

In a previous study [15] we have already focused only on solar protons in the SPE, to evaluate the shielding effectiveness of Bi_2O_3-PMMA—where PMMA stands for polymethyl methacrylate. The material has been proposed as an efficient gamma shield [16], together with similar Bi_2O_3-based materials [17].

2. Simulation Description and Methods

As it has been done before [15], the spectral distribution of solar protons corresponds to the fluence curve vs. energy [MeV] presented by Xapsos *et al.* [9], specifically, experimental points from the 4-August-1972 event. This event has the largest fluence value, among the five events described in the study [9]. Thus, selected for the present study. The fluence profile serves as a guide for the Monte Carlo simulation and a reasonable point of comparison for distinct shielding materials, for instance Bi_2O_3-PMMA vs. aluminum (Al). The latter, the main shielding material of the ISS.

Fluence values were scaled down to 100 events at the neutron energy of 150 MeV, and up to about 77×10^3 events at 10 MeV. In Fig. 1, it is observed that experimentally measured fluence values range from 10^7 to 10^{10} cm^{-2} . Our strategy aims at being implemented with a regular laptop/PC, while also achieving swift convergence to reasonable descriptive results. Only the Bertini-style cascade model has been used to consider hadronic interactions, and the simulation grid has a step size of 0.1 mm.

Physical models used to probe radiation dose are similar to the one here described. There are three layers in the model here used: shield, gap, and muscular tissue. In the simulation the cross section has dimensions of 100×100 cm^2, and the thicknesses of the stack are: shield 100 mm, gap 10 mm, and muscular tissue 100 mm. Shielding thickness is thus comparable to the one at the ISS. The proton beam impinges from the side of the shield, right at its center, and has a punctual dimension. Kinetic energy of the proton beam will vary according to the spectral distribution depicted in Fig. 1.

Typically GEANT4 [18] only requires the density values of the materials which are considered homogeneous—while not employed here, there are some efforts to introduce detailed material structure in the simulations [19]. These were drawn directly from its database—NIST compounds HEP materials. In the present case we have 2.7 gcm^{-3}, 1.204×10^{-3} gcm^{-3}, and 1.050 gcm^{-3}, for aluminum shield, air gap, and muscular tissue, respectively.

The material compared to aluminum in this study, is a composite of PMMA, density = 1.180 gcm^{-3}, with 44 wt.% Bi_2O_3, density = 8.9 gcm^{-3}.

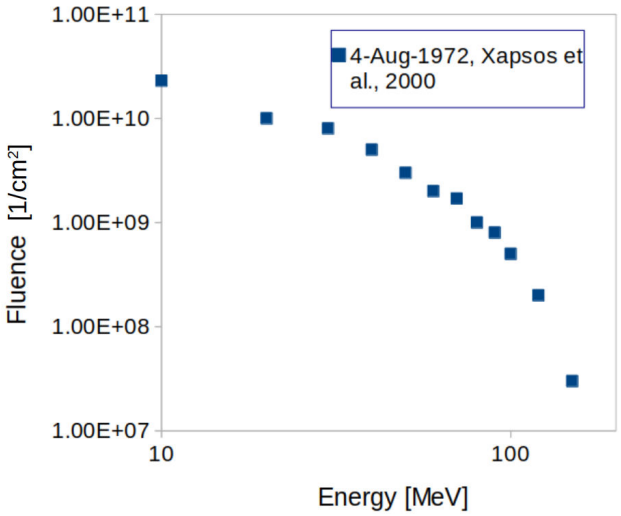

FIGURE 1. Fluence of solar protons used in the simulations here described [15] . This curve corresponds to the solar event from August 4, 1972. Digitized from Xapsos *et al.* [9]. The authors [9] used a function that is equivalent to a Weibull distribution.

The same protocol followed before [15] is followed here:

1. The proton fluence is scaled-down.
2. Neutrons arising as secondary particles are selected from the histograms produced by GEANT4.
3. A reduced shield thickness, t, is calculated from the information at step 2: t = T - d, where: t = reduced shield thickness, T = nominal shield thickness, 100 mm, d = Σ (n(E$_i$) δ(E$_i$)) / Σ n(E$_i$), d = weighed depth of neutron generated as a secondary particle, n(E$_i$) = number of neutrons—secondary particles—with a kinetic energy E$_i$, δ(E$_i$) = depth of creation of neutron—secondary particle—with kinetic energy E$_i$.
4. Estimation of bin size, K, and number of neutron events per bin, N. Bin sizes are estimated using Doane's formula [20]. Bin sizes selected with this formulation are adequate for event distributions that are not normally distributed—our case. K = $1 + \log_2(\eta) + \log_2(1 + |\mu_3|/s)$, where: η = all secondary particles that are neutron events. μ_3 = third standardized moment of skewness, s = $\sqrt{[6(\eta-2)(\eta+1)-1(\eta+3)-1]}$ K will yield the N: N = Σ n(E$_i$), if E$_i$ is within the bin width boundaries.

   Bin width boundaries are established after identifying the maximum and minimum energies and after partitioning the whole energy interval.
5. Computation of the energy value assigned to a bin, ϵ_k. This number is obtained from a simple energy average within those available in the bin, ϵ_k. Such a value represents the kinetic energy of the new set of primary particles, or neutron fluence, used in the subsequent Monte Carlo set of simulations.

6. Identification and recording of all events that deposit energy within the muscular tissue volume.

7. All particles are classified and their respective energies are added up.

8. The factor used to scale down the fluence at step 1 is now used to restore the fluence value.

9. Doses are calculated.

The reduced shield thickness ranged from of 65.704 mm at 150 MeV protons, to 96.966 mm at 50 MeV.

GEANT4 contains various types of interaction models but we only use the Bertini cascade model [21] in the present study, as done before [15] and as already mentioned above.

3. Results and discussion

Recapitulating, our strategy used protons, which are the primary particles that give rise to a proportional fluence of secondaries—neutrons. Because secondaries are produced at various depths, correlated to the energy of the primaries, a reduced thickness is introduced as part of the simulation. Clearly, there is a corresponding fluence value of the secondaries, that stems out of a fluence of primaries, Fig. 1.

Da Cao *et al*. [16] explored experimentally various wt% compositions of Bi_2O_3 and PMMA. We have only explored one composition but will present the rest of them in a subsequent study.

The process described in Sec. 2 yielded the spectral distribution of neutron kinetic energies displayed in Table I. Those energies were estimated after binning secondary particles—neutrons—generated by proton impacts within the radiation shield. Once again, the approach was inspired by the experimental results mentioned above [13]. Neutron radiation is thus expected to be originated by protons from SPE and GCR, although not stated as such in the study of Palvalvi *et al*. [13]. Given their composition we have used only solar protons as primaries, in the interest of having a simplified and systematic approach. Though both SPE and GCR are of concern, from our vantage point within the solar system, SPE are of greater relevance.

Aluminum shielding produced the following particles during the virtual irradiation process: neutron, proton, gamma, alpha, O(16), C(12), N(15), N(14), e-, e+, deuteron, alpha, Be(8), Al(27), Al(26), Mg(26), Mg(25), Mg(24), Ne(22), Ne(21), Na(24), Na(23), and Si(27).

Histograms from GEANT4 yielded information about the type of particle and the energy that each virtual irradiation deposited within each of the layers. Spectral distribution of neutrons is summarized in Table I—values of kinetic energy and thickness have been rounded up.

The simulation indicates that there is a rich contribution to the radiation field due to the shield. We can readily classify the different particles and estimate their respective doses. Figure 2 shows that electrons contribute a larger dose for protons impinging at lower kinetic energies. The dose has a reduction at kinetic energies above 50 MeV. While protons, viewed as secondaries, deposited a fairly uniform dose starting from protons with kinetic energies of 40 MeV.

A lower dose contribution, Fig. 4, is delivered by other particles, which is relatively uniform throughout the range of proton kinetic energies. Alpha, O(16), C(12), neutron, and Be(8) have the highest dose contributions, after protons and electrons (< 40 MeV). Gamma photons have the lowest dose contribution.

TABLE I. The procedure described in Sec. 2 yielded a neutron spectral distribution, *i.e*. binned secondaries resulting from the proton fluence. In addition to the energies of the primary particles we display their associated reduced thickness. Consider that $*$ = kinetic energy of protons, $**$ = shield's reduced thickness, ‡ = kinetic energy of neutrons as secondary particles.

Kinetic Energy(*) [MeV]	**Thickness(**) [mm]**	**Kinetic Energy(‡) [MeV]**
50	96.966	2.912
60	91.940	0.623
		7.290
		26.600
70	90.733	2.395
		10.800
		19.400
		20.500
80	82.809	3.976
		19.900
90	82.319	1.980
		6.910
		33.150
		42.900
100	73.181	2.342
		7.850
		23.867
		49.400
		55.000
120	67.039	2.517
		9.363
		13.100
		28.233
		37.000
		39.300
150	65.704	4.636
		37.750
		68.200
		88.567
		105.000
		137.500

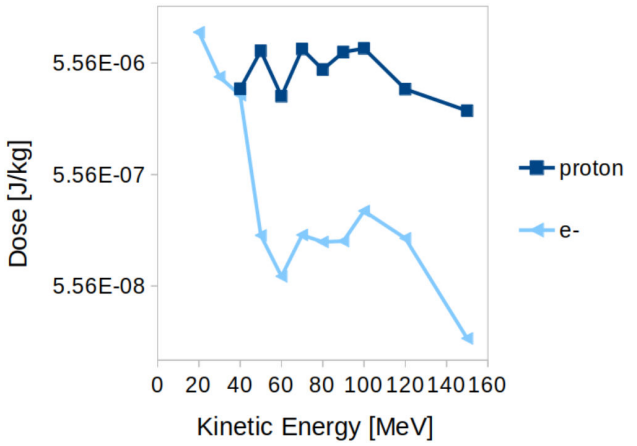

FIGURE 2. Protons and electrons have the largest dose values. Kinetic energies of impinging protons are represented along the horizontal axis, given by SPE precursors.

TABLE II. Dose values by protons and neutrons deposited within the muscular tissue layer were estimated. Values in both columns correspond to secondary particles.

	Dose [J/kg]	Dose [J/kg]
Proton Energy [MeV]	**Proton**	**Neutron**
40	3.2655E-06	1.5903E-07
50	7.1484E-06	1.6545E-07
60	2.7990E-06	4.9574E-08
70	7.4213E-06	1.0467E-07
80	4.8578E-06	6.2410E-08
90	6.9735E-06	9.7842E-08
100	7.5174E-06	1.0503E-07
120	3.2426E-06	4.8796E-08
150	2.0757E-06	1.2465E-08

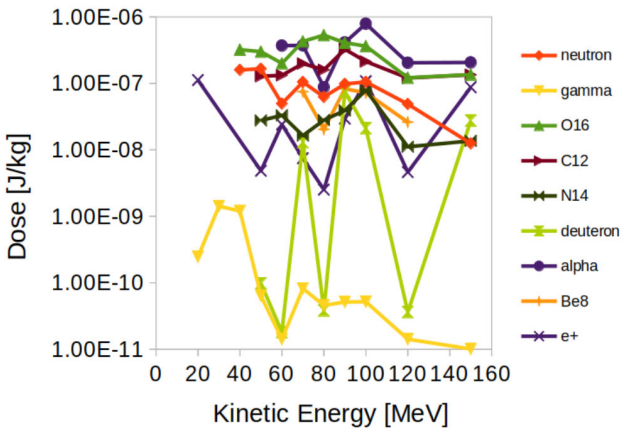

FIGURE 3. Dose deposited in muscular tissue. These values correspond to particles other than protons and neutrons, identified as secondaries. The kinetic energy corresponds to the one from incident protons.

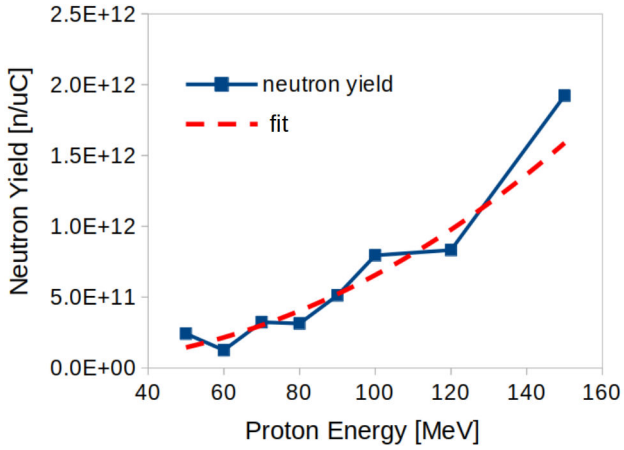

FIGURE 4. Functional dependence between proton energy [MeV] and neutron yield n μC^{-1}, n = neutrons. Experimental values (squares) and a trend line (dashed line) are displayed.

Table II summarizes the dose deposited by protons and neutrons, as secondary particles, with the former depicted at Fig. 2. Dose deposited by other particles are only plotted in Fig. 3.

Considering that the primaries are protons, we create a formulation to represent the neutron yield as a function of proton energy, Fig. 5. Fasil'kov *et al.* [22] produced an empirical formula where the neutron yield is represented in units μC^{-1}, when lead is used as shield. In the present study we also normalized to μC and obtained an expression for the neutron yield, Eq. (1):

$$Y(E) = 28602078.9982E^{2.1830} \quad (1)$$

where $Y(E)$ is the neutron yield and E is the proton energy, Fig. 4. This functional representation resembles the one of Lavelle *et al.* [23]. In the present work the interest was to compare the data trend to results from other authors, who experimentally observed power law trends at various incident-proton energy ranges [22–24]. A power law has a plausible physical representation because the yield is reduced to zero when the proton energy is zero too. A stochastic term could be added, of course, to account for experimental uncertainties, but we have not done so.

From our simulations, protons (secondaries) have the largest average dose. We only note—without calculation—that dose equivalent values can be readily calculated after considering the respective Q factors. Clearly, ions have larger Q factors, thus considered biologically more harmful.

In view of Fig. 5, the reduced thickness corresponding to PMMA-Bi_2O_3, is smaller, which indicates a greater penetration of the proton beam into the shield, at lower proton energies, when compared to aluminum shielding. At the higher energy end of proton energies the reduced thickness has similar values in both shielding types. It is concluded, from the results here observed, that PMMA-Bi_2O_3 brings no shielding advantage under exposure to a proton radiation field. But it could also be argued that it was not really designed as a proton shield. This is an important aspect to note, because any

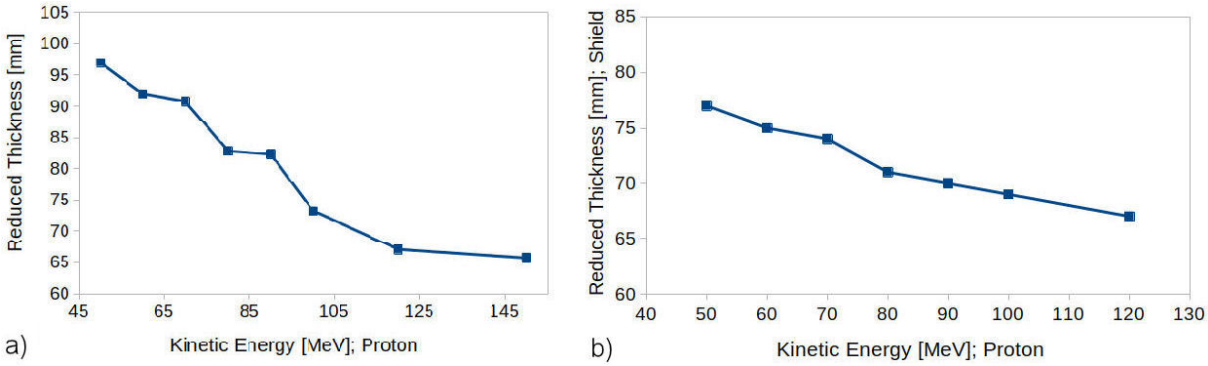

FIGURE 5. a) Dose data from PMMA-Bi_2O_3 were plotted as a function of reduced thickness [15]. b) The curve corresponding to aluminum shielding, shows also the change of reduced thickness respect to proton kinetic energy.

launching into outer space must consider the payload aspect intertwined with radiation shielding.

4. Summary

The model here used is as simple as physical models employed onboard the ISS, or other irradiation studies. Also, we find the methodology suitable for desktop computers. A scaled fluence overcomes the need of fluence values comparable to those registered by experimental measurements [9]. One problem, of course, is the loss of dynamic information as the process happens.

Results from prior work [15] indicate that gamma photons had the smallest dose contribution with PMMA-Bi_2O_3. That is also the case with an aluminum-made shield. Aluminum, unlike PMMA-Bi_2O_3, recorded a gamma dose throughout the whole energy range of SPE. Whether this aspect is an artifact of the methodology or an event that would actually happen experimentally, is something that can not be answered at this time. However, it can be stressed that PMMA-Bi_2O_3 was designed as a gamma shield [16].

The functional relationship, Eq. (1), between proton fluence and neutron yield displays an expected increase with energy. In the present case, however, the neutron yield does not display a decrease typically due to target transparency observed at a spallation neutron source. Here the trend is as observed because the energy is not large enough, commensurate with the target thickness. It is expected that the functional relationship here identified, can serve as an experimental guide to shielding design in a proton field.

Unfortunately, the work of Palfalvi *et al.* [13] did not classify ion dose information but only the neutron dose. It is here proposed, that a methodology like the one used by Jeong *et al.* [25] onboard an extraterrestrial probe, exposed to SPE, could serve as an experimental comparison benchmark for the results here presented. Such a setup could also be simulated using GEANT4.

Acknowledgments and disclaimer

Financial support to present the findings in this article was provided to the authors by the SMF. The views and opinions in this article are those of the author(s) and do not necessarily reflect the views and opinions of Bruker AXS or any of its affiliates.

1. R. Francis *et al.*, AEGIS Autonomous Targeting for ChemCam on Mars Science Laboratory: Deployment and Results of Initial Science Team Use, *Sci. Robot.* **2** (2017) 1, https://doi.org/10.1126/scirobotics.aan4582.

2. K. W. Lewis *et al.*, A Surface Traverse on Mars Indicates Low Bedrockdensity at Gale Crater, *Science* **363** (2019) 535, https://doi.org/10.1126/science.aat0738.

3. P. E. Rosen, D. Zhang, J. H. Jiang, L. V. Ijzendoorn, K. A. Fahy, and Z.-H. Zhu, Impact of Economic Constraints on the Projected Timeframe for Human-Crewed Deep Space Exploration, *Galaxies* **10** (2022) 1, https://doi.org/10.3390/galaxies10040088.

4. M. Weinzierl and M. Sarang, The Commercial Space Age Is Here, *Harv. Bus. Rev.* (2021). https://hbr.org/2021/02/the-commercial-space-age-is-here.

5. A. J. Taylor, J. C. McDowell, and M. Elvis, Phobos and Mars Orbit as a Base for Asteroid Exploration and Mining, *Planet. Space Sci.* **214** (2022) 105450, https://doi.org/10.1016/j.pss.2022.105450.

6. H. G. Changela *et al.*, Mars: New Insights and Unresolved Questions, *Int. J. Astrobiol.* **20** (2021) 394, https:/doi.org/10.1017/S1473550421000276.

7. J. W. Wilson, F. A. Cucinotta, J. L. Shinn, M.-H. Kim, and F. F. Badavi, Preliminary Considerations, in Shielding Strategies for Human Space Exploration (Houston, TX, U.S.A., 1997).

8. S. Thoudam, J. P. Rachen, A. van Vliet, A. Achterberg, S. Buitink, H. Falcke, and J. R. Hörandel, Cosmic-Ray

Energy Spectrum and Composition up to the Ankle - the Case for a Second Galactic Component, *Astron. Astrophys.* **595** (2016) A33, https://doi.org/10.1051/0004-6361/201628894.

9. M. A. Xapsos, J. L. Barth, E. G. Stassinopoulos, S. Messenger, G. P. Summers, and E. A. Burke, Characterizing Solar Proton Energy Spectra for Radiation Effects Applications, *Nucl. Sci. IEEE Trans. On* **47** (2001) 2218, https://doi.org/10.1109/23.903756.
10. L. Miroshnichenko, Retrospective Analysis of GLEs and Estimates of Radiation Risks, *J. Space Weather Space Clim.* **8** (2018) A52. httsp://doi.org/10.1051/swsc/2018042.
11. T. Berger *et al*., DOSIS & DOSIS 3D: Long-Term Dose Monitoring Onboard the Columbus Laboratory of the International Space Station (ISS), *J. Space Weather Space Clim.* **6** (2016) A39. https://doi.org/10.1051/swsc/2016034.
12. L. E. Wahl, Environmental Radiation Fact Sheet 2010, No. Fact Sheet: January 2010, *Health Physics Society*, 2010. https://hps.org/documents/environmental_radiation_fact_sheet.pdf.
13. J. K. Pàlfalvi, Y. Akatov, J. Szabó, L. Sajo-Bohus, and I. Eördögh, Detection of Primary and Secondary Cosmic Ray Particles Aboard the ISS Using SSNTD Stacks, *Radiat. Prot. Dosimetry* **120** (2006) 427, https://doi.org/10.1093/rpd/nci673.
14. J. T. Wilson, D. J. Lawrence, P. N. Peplowski, V. R. Ecke, and J. A. Kegerreis, Space-Based Measurement of the Neutron Lifetime Using Data from the Neutron Spectrometer on NASA's MESSENGER Mission, *Phys. Rev. Res.* **2** (2020) 023316, https://doi.org/10.1103/PhysRevResearch.2.023316.
15. L. Sajo-Bohus, J. A. López, and M. Castro-Colin, Simulation of Dose Estimations from Solar Protons: A PMMA-Bi2O3 Shielding Model for Space Exploration, *J. Nucl. Phys. Mater. Sci. Radiat. Appl*. **8** (2021) 155, https://doi.org/10.15415/jnp.2021.82020.
16. D. Cao, G. Yang, M. Bourham, and D. Moneghan, Gamma Radiation Shielding Properties of Poly (Methyl Methacrylate) / Bi_2O_3 Composites, *Nucl. Eng. Technol*. **52** (2020) 2613, https://doi.org/10.1016/j.net.2020.04.026.
17. S. A. M. Issa, M. Ahmad, H. O. Tekin, Y. B. Sadeek, and M. I. Sayyed, Effect of Bi2O3 Content on Mechanical and Nuclear Radiation Shielding Properties of Bi2O3-MoO3-B2O3-SiO2-Na2O-Fe2O3 Glass System, *Results Phys.* **13** (2019) 102165, https://doi.org/10.1016/j.rinp.2019.102165.
18. S. Agostinelli *et al*., Geant4-a Simulation Toolkit, *Nucl. Instrum. Methods Phys. Res. Sect. Accel.* Spectrometers Detect. *Assoc. Equip.* **506** (2003) 250, https://doi.org/10.1016/S0168-9002(03)01368-8.
19. E. Bagli, M. Asai, A. Dotti, L. Pandola, and M. Verderi, Allowing for Crystalline Structure Effects in Geant4, *Nucl. Instrum. Methods Phys. Res. Sect. B Beam Interact. Mater. At.* **402** (2017) 304. https://doi.org/10.1016/j.nimb.2017.03.092
20. D. P. Doane, Aesthetic Frequency Classifications, *Am. Stat.* **30** (1976) 181,
21. D. H. Wright and M. H. Kelsey, The GEANT4 Bertini Cascade, *Nucl. Instrum. Methods Phys. Res. A* **804** (2015) 175, https://doi.org/10.1016/j.nima.2015.09.058.
22. R. G. Fasil'kov, N. S. Mysin, and Y. M. Chirkin, Neutron Yield from a Massive Lead Target under the Action of Relativistic Light Ions, *At. Energy* **79** (1995) 664, https://doi.org/10.1007/BF02415388.
23. C. M. Lavelle *et al*., Neutronic Design and Measured Performance of the Low Energy Neutron Source (LENS) Target Moderator Reflector Assembly, Arxiv arXiv:0803.4170, (2008). https://arxiv.org/abs/0803.4170.
24. R. R. Fullwood, J. D. Cramer, R. A. Haarman, R. P. Forrest Jr., and R. G. Schrandt, Neutron Production by Medium-Energy Protons on Heavy Metal Targets, No. LA-4789, Los Alamos Sci. Lab., 1972.
25. T. W. Jeong *et al*., CR-39 Track Detector for Multi-MeV Ion Spectroscopy, *Sci. Rep.* **7** (2017) 1. https://doi.org/10.1038/s41598-017-02331-w.